DELFT UNIVERSITY OF TECHNOLOGY

REPORT 18-2

Conservative Taylor Least Squares reconstruction for material point methods

E. Wobbes, M. Möller, V. Galavi, and C. Vuik

ISSN 1389-6520

Reports of the Delft Institute of Applied Mathematics

Delft 2018

Abstract

Within the standard Material Point Method (MPM), the spatial errors are partially caused by the direct mapping of material-point data to the background grid. In order to reduce these errors, we introduced a novel technique that combines the Least Squares method with the Taylor basis functions, called Taylor Least Squares (TLS), to reconstruct functions from scattered data. The TLS technique locally approximates quantities of interest, such as stress and density, and when used with a suitable quadrature rule, conserves the total mass and linear momentum after transferring the material-point information to the grid. For one-dimensional examples, applying the TLS approximation significantly improves the results of MPM, Dual Domain Material Point Method (DDMPM), and B-spline MPM (BSMPM). Due to its outstanding conservation properties, the TLS technique outperforms the nonconservative reconstruction techniques, such as spline reconstruction. For example, in contrast to the solution generated using the global cubic-spline interpolation, the TLS solution satisfies the boundary conditions of a two-phase benchmark. Therefore, the TLS reconstruction increases the accuracy of the material point methods, while preserving the fundamental physical properties of the standard algorithm.

1 Introduction

The Material Point Method (MPM) [1, 2] is a continuum-based numerical tool to simulate problems that involve large deformations. In MPM, the material is represented by a set of Lagrangian particles (material points) that move through a fixed Eulerian background grid. The material points carry the physical properties of the continuum such as the mass, strain, and stress. At the beginning of each time step, this information is projected from the particles to the degrees of freedom (DOFs) of the background grid, where similarly to the Finite Element Method [3] (FEM), the discretised governing equations are assembled and subsequently solved. The obtained information is then mapped back to update the material points. This conjunction of Lagrangian and Eulerian approaches makes MPM well-suited for challenging problems involving large strains.

Despite its impressive performance for many engineering problems [4, 5], standard MPM still suffers from several shortcomings. For example, when large deformations are considered, the particular case of Shepard interpolation [6] used by the method to project the scattered material-point data to the DOFs can introduce significant numerical inaccuracies [7, 8]. In addition, when material points travel from one cell to another, they generate unphysical oscillations in the forces, frequently referred to as grid-crossing error [9]. This is due to the use of piecewise-linear basis functions, whose gradients are discontinuous on element boundaries. Finally, MPM contains FEM-type errors originating from mass-lumping and interpolation, as well as time-stepping errors [10].

Much research has been conducted to overcome these shortcomings. On the one hand, methods such as the Generalized Interpolation Material Point (GIMP) method [9], the Convected Particle Domain Interpolation (CPDI) method [11], the Dual Domain Material Point method (DDMPM)[12], and the B-Spline Material Point Method (BSMPM) [13, 14] have been designed to overcome the grid-crossing error. On the other hand, Sulsky and Gong [7, 8] have shown that the shortcomings resulting from the mapping of particle information can be decreased by reconstructing functions with a higher-order technique, such as a Moving Least Squares approximation, and evaluating these functions at the desired positions. Furthermore, Tielen et al. [14] have pointed out that the use of global cubic-spline function reconstruction technique substantially improves the performance of BSMPM. Although modified mapping generally improves the accuracy of the solution, the standard reconstruction techniques might lead to the loss of physical properties of the material point methods. In fact, while MPM projection conserves the mass and linear momentum of the system, most standard mapping techniques do not guarantee that. Therefore, more advanced solutions are required for function reconstruction.

In this paper, we propose a novel Taylor Least Squares (TLS) reconstruction technique, which is based on the Least Squares [15] approximation constructed from a set of Taylor basis functions [16]. This technique reconstructs quantities of interest such as stress, pore pressure, and density locally, within each active cell, and evaluates them at the integration points. After that, a Gauss quadrature is applied to determine the internal forces and velocities. If a sufficient number of Gauss points is defined within each element, the proposed mapping technique preserves the physical qualities of the standard MPM by conserving

the mass and linear momentum of the system.

While the TLS reconstruction can be used autonomously, it can also be combined with methods like GIMP or BSMPM in order to further reduce the spatial errors. Since previous studies have indicated that DDMPM and BSMPM are viable alternatives not only for MPM, but also for GIMP and CPDI [12, 17, 18], we have applied the TLS reconstruction technique within MPM, DDMPM, and BSMPM. The methods are tested on two benchmarks describing the deformation of a one-phase vibrating bar and consolidation of a two-phase porous material in one spatial dimension. The quality of the TLS conservative properties are verified by computing the total mass and momentum before and after projecting the particle information to the background grid. Depending on the availability of the analytical solution, the accuracy of the material point methods with TLS approximation is investigated either qualitatively or based on the spatial errors and convergence rates. In addition, the obtained results are compared to those computed with the cubic-spline reconstruction technique [14].

We observe that when grid crossing does not occur, the TLS reconstruction technique has little influence on MPM, but can significantly improve the convergence of DDMP and BSMPM. When particles start to cross element boundaries, the effect of the advanced reconstruction technique becomes clearly evident for all considered methods. In fact, the TLS technique smoothens their solutions and ensures that the boundary conditions are satisfied. Moreover, the TLS approximation outperforms the global spline interpolation in terms of conservation of the mass and momentum and the preservation of the boundary conditions. Therefore, the TLS reconstruction leads to a conservative projection of the particle data and increases the accuracy of the material point methods.

This paper is structured as follows. Section 2 introduces the governing equations capturing the one-dimensional deformation of one- and two-phase continua. Section 3 summarises the MPM algorithm to numerically discretise and solve these equations and outlines the modifications required to obtain DDMPM. Section 4 focuses on the use of B-splines in MPM. Section 5 describes the main concepts of the TLS reconstruction and proves that its use with a sufficiently accurate Gauss quadrature leads to a conservative data projection. Section 6 discusses the numerical results obtained for vibrating bar and consolidation problems. Finally, Section 7 provides the conclusions.

2 Governing equations

2.1 One-phase continuum

In this paper, it is assumed that the considered continuum occupies a domain $\Omega_0 \subseteq \mathbb{R}$ at time t_0 and a domain $\Omega \subseteq \mathbb{R}$ at time $t > t_0$. The material does not undergo irreversible deformations. One-dimensional deformations of such a continuum can be described for small strains by a closed coupled system of partial differential equations for velocity and

stress in the following manner [19]:

$$\rho \frac{\partial v}{\partial t} = \frac{\partial \sigma}{\partial x} - \rho g, \tag{1}$$

$$\frac{\partial \sigma}{\partial t} = E \frac{\partial v}{\partial x}. \tag{2}$$

The coordinate x refers to the spatial direction, while t denotes the time. Moreover, ρ is the density, v is the velocity, σ is the stress tensor, g is the gravitational acceleration, and E is Young's modulus.

Equation (1) is obtained from the momentum balance equation, whereas Equation (2) describes the linear elastic constitutive relation for small strains. For large deformations, Equation (2) needs to be replaced by [20]

$$\frac{\partial \sigma}{\partial t} = (E - \sigma) \frac{\partial v}{\partial x}. \tag{3}$$

This system can be extended by a relation between the velocity v and displacement u given by

$$v = \frac{\partial u}{\partial t}. \tag{4}$$

In order to obtain a unique solution to the above system of equations, initial and boundary conditions have to be prescribed. Therefore, the following initial conditions are required:

$$u(x,0) = u_0(x), \quad v(x,0) = v_0(x), \quad \sigma(x,0) = \sigma_0(x) \quad \forall\, x \in \Omega_0.$$

In addition, two types of boundary conditions are considered:

- Dirichlet boundary conditions (i.e., $u(x,t) = \hat{u}(t)$ for $x \in \partial\Omega_u$);
- Neumann boundary conditions (i.e., $\sigma(x,t) = \tau(t)$ for $x \in \partial\Omega_\tau$).

2.2 Two-phase continuum

According to the $v-w$ formulation [21], one-dimensional deformations of a saturated two-phase continuum are described for small strains by the following closed coupled system of equations:

$$\rho_w \frac{\partial v_w}{\partial t} = \frac{\partial p}{\partial x} - \frac{n\gamma_w}{k}(v_w - v_s) - \rho_w\, g, \tag{5}$$

$$(1-n)\rho_s \frac{\partial v_s}{\partial t} = -n\rho_w \frac{\partial v_w}{\partial t} + \frac{\partial \sigma}{\partial x} - \rho_{sat} g, \tag{6}$$

$$\frac{\partial p}{\partial t} = \frac{K_w}{n}\left((1-n)\frac{\partial v_s}{\partial x} + n\frac{\partial v_w}{\partial x}\right), \tag{7}$$

$$\frac{\partial \sigma'}{\partial t} = E^c \frac{\partial v_s}{\partial x}, \tag{8}$$

$$\sigma = \sigma' + p. \tag{9}$$

In the above, ρ_w is the density of the liquid phase, v_w is the velocity of the liquid phase, p is the pore pressure, n is the porosity, γ_w is the unit weight of the liquid phase, k is the Darcy permeability, v_s is the velocity of the solid phase, g is the gravitational acceleration, ρ_s is the velocity of the solid state, σ is the total stress, ρ_{sat} is the saturated density, K_w is the bulk modulus of the liquid phase, E^c is the constrained modulus, and σ' is the effective stress [22].

The equations are based on the conservation of momentum for the liquid phase, the conservation of momentum and mass for the mixture of the solid and liquid phase, the constitutive equation, and the definition of effective stress. For large strains, Equation (8) is replaced by [20]

$$\frac{\partial \sigma'}{\partial t} = (E^c - \sigma') \frac{\partial v_s}{\partial x}. \tag{10}$$

The displacement of the solid phase u_s can be included in the formulation using the following relation:

$$v_s = \frac{\partial u_s}{\partial t}. \tag{11}$$

This system of equations needs to satisfy the initial and boundary conditions. The initial conditions read

$$\begin{aligned} u_s(x,0) = u_{s,0}(x), \quad v_s(x,0) = v_{s,0}(x), \quad \sigma(x,0) = \sigma_0(x) \quad \forall\, x \in \Omega_0; \\ v_w(x,0) = v_{w,0}(x), \quad p(x,0) = p_0(x) \quad \forall\, x \in \Omega_0. \end{aligned}$$

For both phases, Dirichlet and Neumann boundary conditions are considered. The Dirichlet boundary conditions are given by

$$\begin{aligned} u_s(x,t) = \hat{u}_s(t) \text{ for } x \in \partial\Omega_{u_s}, \\ v_w(x,t) = \hat{v}_w(t) \text{ for } x \in \partial\Omega_{v_w}, \end{aligned}$$

whereas the Neumann boundary conditions can be written as

$$\begin{aligned} \sigma(x,t) = \tau(t) \text{ for } x \in \partial\Omega_\tau, \\ p(x,t) = \hat{p}(t) \text{ for } x \in \partial\Omega_p. \end{aligned}$$

3 Low-order material point methods

3.1 Discretisation

The momentum balance equation of a one-phase continuum (Equation 1) is solved by MPM [7, 8] in its weak formulation:

$$\int_\Omega \delta v \rho \frac{\partial v}{\partial t} d\Omega = \delta v \sigma \Big|_{\partial\Omega} - \int_\Omega (\nabla \delta v) \sigma d\Omega - \int_\Omega \delta v \rho g d\Omega,$$

where δv denotes a test function.

We introduce vector notation for quantities defined at the DOFs to simplify the description. If the domain discretisation generates N_n DOFs, we denote the velocity vector by $\mathbf{v}(t) = [v_1(t)\ v_2(t)\ \dots\ v_{N_n}(t)]^T$. The basis function vector is given by $\boldsymbol{\phi}(x) = [\phi_1(x)\ \phi_2(x)\ \dots\ \phi_{N_n}(x)]^T$, where ϕ_i represents a basis function centred at the ith DOF. Thus, the velocity is approximated according to the finite-element approach:

$$v(x,t) \approx \boldsymbol{\phi}(x)^T \mathbf{v}(t).$$

The displacement u and virtual velocity δv are discretised in a similar way.

The semi-discretised weak formulation can then be written as

$$\int_\Omega \rho \boldsymbol{\phi}\boldsymbol{\phi}^T \frac{d\mathbf{v}}{dt} = \sigma(x,t)\boldsymbol{\phi}\Big|_{\partial\Omega} - \int_\Omega \rho g \boldsymbol{\phi}\, d\Omega - \int_\Omega \sigma(x,t)\nabla\boldsymbol{\phi}\, d\Omega.$$

Denoting the acceleration vector $\mathbf{a} = \frac{d\mathbf{v}}{dt}$, the consistent mass matrix $M^C = \int_\Omega \rho\boldsymbol{\phi}\boldsymbol{\phi}^T d\Omega$, the external force vector $\mathbf{f}^{\text{ext}} = \sigma(x,t)\boldsymbol{\phi}\Big|_{\partial\Omega} - \int_\Omega \rho g\boldsymbol{\phi}\, d\Omega$, and the internal force vector $\mathbf{f}^{\text{int}} = \int_\Omega \sigma(x,t)\nabla\boldsymbol{\phi}\, d\Omega$, we obtain

$$M^C\mathbf{a} = \mathbf{f}^{\text{ext}} - \mathbf{f}^{\text{int}}. \tag{12}$$

It should be noted that in the considered version of MPM, the consistent mass matrix in Equation (12) is typically replaced by the lumped mass matrix, which is obtained by summing off-diagonal entries of M^C, $M = \int_\Omega \rho\boldsymbol{\phi} d\Omega$. Alternatively, the lumping can be performed variationally. Thus, the mass corresponding to the DOFs is stored in the diagonal $\mathbf{m}$ of M:

$$M = \begin{bmatrix} \ddots & & \\ & \mathbf{m} & \\ & & \ddots \end{bmatrix}.$$

Finally, the stress is updated using the gradient of the basis function vector $\nabla\boldsymbol{\phi}(x)$ and the constitutive relation. For example, for small deformations, Equation (2) yields:

$$\sigma(x,t) \approx E\nabla\boldsymbol{\phi}(x)^T\mathbf{u}(t). \tag{13}$$

In MPM, the particles move within the grid and serve as integration points. If the continuum is discretised by N_p material points, then for an arbitrary function f, the integral is computed as

$$\int_\Omega f(x)d\Omega \approx \sum_{p=1}^{N_p} V_p f(x_p),$$

where V_p is the particle volume.

For temporal discretisation the considered version of MPM adapts the Euler-Cromer time-stepping scheme [23]. This method is semi-implicit, applying the forward Euler method to advance the velocity in time and the backward Euler method to advance the

displacement. The scheme is energy conservative, conditionally stable, and first-order accurate.

The discretisation of the two-phase formulation from Section 2.2 is similar to that described above. The spatial discretisation results in the following system:

$$M_w^C \mathbf{a}_w = \mathbf{f}_w^{\text{ext}} - \mathbf{f}_w^{\text{int}},$$
$$M_s^C \mathbf{a}_s + \bar{M}_w^C \mathbf{a}_w = \mathbf{f}_s^{\text{ext}} - \mathbf{f}_s^{\text{int}},$$

where M_w^C, M_s^C, and $\bar{M}_w^C$ are the consistent mass matrices, $\mathbf{a}_w$ and $\mathbf{a}_s$ are the acceleration vectors, and $\mathbf{f}_w^{\text{ext}}$, $\mathbf{f}_w^{\text{int}}$, $\mathbf{f}_s^{\text{ext}}$, and $\mathbf{f}_s^{\text{int}}$ are the force vectors for the liquid and solid phase, respectively. The corresponding lumped mass matrices have the following forms:

$$M_w = \begin{bmatrix} \diagdown & \\ & \mathbf{m_w} \\ & & \diagdown \end{bmatrix}, \quad M_s = \begin{bmatrix} \diagdown & \\ & \mathbf{m_s} \\ & & \diagdown \end{bmatrix}, \quad \bar{M}_w = \begin{bmatrix} \diagdown & \\ & \bar{\mathbf{m}}_w \\ & & \diagdown \end{bmatrix}.$$

For more details of the discretisation, the reader is referred to [24].

3.2 Algorithm for one-phase continuum

When the deformation of a one-phase continuum is studied, each particle carries a certain volume V_p, density ρ_p, position x_p, velocity v_p, and stress σ_p. All these values are time-dependent, while the material-point mass m_p is constant throughout the simulation. The superscript t denotes the time level, and Δt is the time step length. At $t = 0$ s, the material points are initialised (see [24] for further details). Assuming that all particle properties are known at time t, the computation for time $t + \Delta t$ proceeds as follows.

First, the data from the material points is projected to the DOFs. For example, the diagonal of the lumped mass matrix and the internal force vector are computed as

$$\mathbf{m}^t = \sum_{p=1}^{N_p} m_p \boldsymbol{\phi}\left(x_p^t\right), \tag{14}$$

$$\left(\mathbf{f}^{\text{int}}\right)^t = \sum_{p=1}^{N_p} \sigma_p^t \cdot \nabla \boldsymbol{\phi}\left(x_p^t\right) V_p^t. \tag{15}$$

The accelerations at the DOFs are then obtained by combining the internal forces with any external forces, namely,

$$\mathbf{a}^t = \left(M^t\right)^{-1} \left(\left(\mathbf{f}^{\text{ext}}\right)^t - \left(\mathbf{f}^{\text{int}}\right)^t\right).$$

While for each DOF, the Update-Stress-Last (USL) scheme [1] calculates the velocities directly from the accelerations, the Modified-Update-Stress-Last (MUSL) scheme [2] computes the particle velocities first and then maps the information to the DOFs. Since USL

can generate ill-conditioned mass matrices when piecewise-linear basis functions are used, we consider the MUSL scheme. Therefore, in the next step, the velocity of particle p at $t + \Delta t$ is determined as

$$v_p^{t+\Delta t} = v_p^t + \Delta t\, \boldsymbol{\phi}^T \left(x_p^t\right)\, \mathbf{a}^t \quad \forall\, p = \{1, 2, \ldots, N_p\}.$$

The velocities at the DOFs are subsequently obtained from

$$\mathbf{v}^{t+\Delta t} = \left(M^t\right)^{-1} \sum_{p=1}^{N_p} m_p \boldsymbol{\phi}\left(x_p^t\right) v_p^{t+\Delta t}. \tag{16}$$

This allows for computing the incremental displacement vector as

$$\boldsymbol{\Delta}\mathbf{u}^{t+\Delta t} = \Delta t\, \mathbf{v}^{t+\Delta t}.$$

After these steps, the remaining part of the particle properties is updated:

$$\begin{aligned} u_p^{t+\Delta t} &= u_p^t + \boldsymbol{\phi}^T \left(x_p^t\right)\, \boldsymbol{\Delta}\mathbf{u}^{t+\Delta t}, \\ x_p^{t+\Delta t} &= x_p^t + \boldsymbol{\phi}^T \left(x_p^t\right)\, \boldsymbol{\Delta}\mathbf{u}^{t+\Delta t}, \\ \Delta\epsilon_p^{t+\Delta t} &= \nabla\boldsymbol{\phi}^T \left(x_p^t\right)\, \boldsymbol{\Delta}\mathbf{u}^{t+\Delta t}, \end{aligned}$$

where u_p and $\Delta\epsilon_p$ are the particle displacement and incremental strain, respectively. The particle stress at $t + \Delta t$ is computed from σ^t and $\Delta\epsilon_p^{t+\Delta t}$ using a constitutive law. Since, only one-dimensional elastic deformations are considered, it follows from Equation (2), (3), and (13) that

$$\sigma_p^{t+\Delta t} = \begin{cases} \sigma_p^t + E\, \Delta\epsilon_p^{t+\Delta t} & \forall\, p = \{1, 2, \ldots, N_p\} \quad \text{for small strains,} \\ \sigma_p^t + \left(E - \sigma_p^t\right)\, \Delta\epsilon_p^{t+\Delta t} & \forall\, p = \{1, 2, \ldots, N_p\} \quad \text{for large strains.} \end{cases}$$

Finally, the volume and density of each particle are computed from

$$\begin{aligned} V_p^{t+\Delta t} &= \left(1 + \varepsilon_p^{t+\Delta t}\right) V_p^t, \\ \rho_p^{t+\Delta t} &= \frac{\rho_p^t}{\left(1 + \Delta\varepsilon_p^{t+\Delta t}\right)}. \end{aligned}$$

3.3 Algorithm for two-phase continuum

For a saturated two-phase continuum described by the $v - w$ formulation from Section 2.2, the information about both phases is assigned to the material points. This implies that every particle carries the following properties: permeability k_p, porosity n_p, density of the solid phase $(\rho_s)_p$, density of the liquid phase $(\rho_w)_p$, volume V_p, position of the solid phase x_p, velocity of the solid phase $(v_s)_p$, velocity of the liquid phase $(v_w)_p$, effective stress σ'_p, and pore water pressure p_p. The above quantities can vary in time, whereas the particle masses for the solid phase, $(m_s)_p$, and liquid phase, $(m_w)_p$, are constant.

Similarly to the algorithm for the one-phase formulation, at the beginning of a computational cycle the information is mapped from the particles to the nodes. For example, the diagonals of M_w, $\bar{M}_w$, and M_s are calculated as follows:

$$\mathbf{m}_w^t = \sum_{p=1}^{N_p} (m_w)_p \, \boldsymbol{\phi}\left(x_p^t\right),$$

$$\bar{\mathbf{m}}_w^t = \sum_{p=1}^{N_p} n_p^t \, (m_w)_p \, \boldsymbol{\phi}\left(x_p^t\right),$$

$$\mathbf{m}_s^t = \sum_{p=1}^{N_p} \left(1 - n_p^t\right) (m_s)_p \, \boldsymbol{\phi}\left(x_p^t\right).$$

The internal forces at the DOFs are obtained from

$$\left(\mathbf{f}_w^{\text{int}}\right)^t = \sum_{p=1}^{N_p} p_p^t \cdot \nabla \boldsymbol{\phi}\left(x_p^t\right) V_p^t,$$

$$\left(\mathbf{f}_s^{\text{int}}\right)^t = \sum_{p=1}^{N_p} \sigma_p'^t \cdot \nabla \boldsymbol{\phi}\left(x_p^t\right) V_p^t.$$

For the two-phase formulation, the presence of the drag force is essential. It is a resistance force acting on the liquid phase due to its relative motion with respect to the solid phase. Thus, this force is included in the computation through f_w^{ext}. The vector containing the drag forces at the DOFs, $\mathbf{f}_w^{drag}$, is given by

$$\left(\mathbf{f}_w^{drag}\right)^t = \sum_{p=1}^{N_p} \frac{n_p^t \, (m_w)_p \, g}{k_p^t} \left(\mathbf{v}_s^t - \mathbf{v}_w^t\right),$$

where g is the gravitational acceleration.

The discretised momentum balance equations provide the accelerations at DOFs for both phases:

$$\mathbf{a}_w^t = \left(M_w^t\right)^{-1} \left(\left(\mathbf{f}_w^{\text{ext}}\right)^t - \left(\mathbf{f}_w^{\text{int}}\right)^t\right),$$

$$\mathbf{a}_s^t = \left(M_s^t\right)^{-1} \left(\left(\mathbf{f}_s^{\text{ext}}\right)^t - \left(\mathbf{f}_s^{\text{int}}\right)^t - \bar{M}_w^t \mathbf{a}_w^t\right).$$

For the solid phase, the remaining part of the method is similar to that from Section 3.2. The only difference is that m_p and σ_p should be replaced by $\left(1 - n_p^t\right)(m_s)_p$ and σ_p', respectively. For the liquid phase, the velocities are calculated as

$$(v_w)_p^{t+\Delta t} = (v_w)_p^t + \Delta t \, \boldsymbol{\phi}^T\left(x_p^t\right) \, \mathbf{a}_w^t \qquad \forall \, p = \{1, 2, \ldots, N_p\},$$

$$\mathbf{v}_w^{t+\Delta t} = \left(\bar{M}_w^t\right)^{-1} \sum_{p=1}^{N_p} n_p^t \, (m_w)_p \, \boldsymbol{\phi}\left(x_p^t\right) (v_w)_p^{t+\Delta t}.$$

Finally, the pore water pressure is obtained from

$$p_p^{t+\Delta t} = p_p^t + \Delta t \, \frac{K_w}{n_p^t} \nabla \boldsymbol{\phi}^T \left(x_p^t\right) \, \left((1 - n_p^t) \, \mathbf{v}_s^{t+\Delta t} + n_p^t \, \mathbf{v}_w^{t+\Delta t} \right) \quad \forall \, p = \{1, 2, \ldots, N_p\}.$$

3.4 Piecewise-linear basis functions

The standard MPM uses piecewise-linear (P1) basis functions illustrated in Figure 1a. On the one hand, P1 basis functions have several advantages:

- They satisfy the partition of unity property:

$$\sum_{i=1}^{N_n} \phi_i(x) = 1 \quad \forall \, x.$$

- Each ϕ_i has compact support. For $i = 2, 3, \ldots, N_n - 1$, ϕ_i is supported by element $i - 1$ and i. The compact supports of basis functions ϕ_1 and ϕ_{N_n} are contained in element 1 and $N_n - 1$, respectively.
- P1 basis functions are implemented in a straightforward manner.
- They enable lumping.

On the other hand, the gradients of the piecewise-linear basis functions, just as the gradients of all other C^0-continuous basis functions, are discontinuous on the element boundaries leading to unphysical oscillations in the internal forces when material points cross those boundaries. The gradient of a P1 function is shown as $\nabla\phi$ in Figure 1b.

3.5 Dual Domain Material Point method

DDMPM [12] uses piecewise-linear basis functions, but replaces their gradients by smoother ones. For the construction of the new gradients, the method introduces a weight function α and the gradient $\widetilde{\nabla\phi_i}$ defined as

$$\widetilde{\nabla\phi_i}(x) = \sum_{j=1}^{N_n} \frac{\phi_j(x)}{V_j} \int_\Omega \phi_j \nabla\phi_i d\Omega,$$

where V_j is the volume associated with node j and given by $V_j = \int_\Omega \phi_j d\Omega$. The weight function is required to be zero on the cell boundaries, but is not uniquely specified [12]. For the one-dimensional problems considered in this paper, the following expression is adopted:

$$\alpha(x) = 2 \sum_{i=1}^{N_n - 1} \phi_i(x) \phi_{i+1}(x).$$

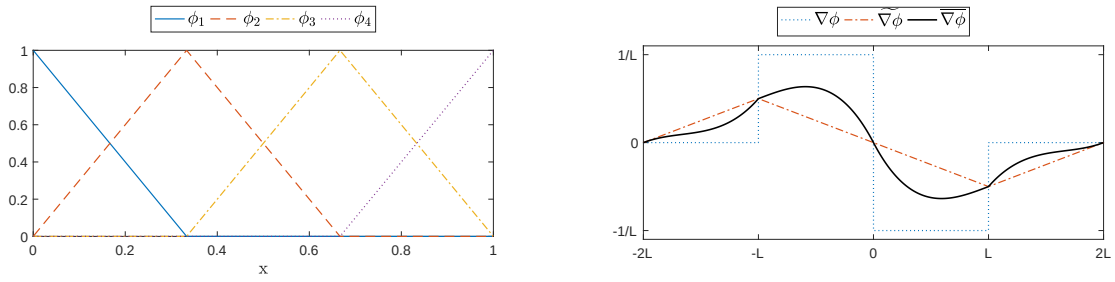

(a) (b)

Figure 1: Piecewise-linear basis functions (a) and basis function gradients used in DDMPM (b). Here, L represents the element length.

DDMPM substitutes the gradients of the piecewise-linear basis functions by

$$\overline{\nabla\phi}_i(x) = \alpha(x)\nabla\phi_i(x) + (1-\alpha(x))\widetilde{\nabla\phi}_i(x) \quad \forall i = \{1,\dots,N_n\},$$

The gradients used in this method are depicted in Figure 1b. Moreover, from Section 3.2 and 3.3 it follows that DDMPM modifies the computation of the internal forces, strains, and pore pressures.

4 B-Spline Material Point Method

BSMPM [13, 14] replaces the piecewise-linear basis functions from Section 3 by higher-order B-splines, which guarantee at least C_0-continuity of the gradients. The use of higher-order B-splines not only reduces the grid-crossing error, but also the interpolation and time-stepping errors [10]. Similarly to piecewise-linear basis functions, B-splines enable lumping of the mass matrix.

B-spline basis functions are constructed based on a *knot vector*, a sequence of ordered nondecreasing points in $\mathbb{R}$ called *knots*. A knot vector is denoted by $\Xi = \{\xi_1, \xi_2, \dots, \xi_{n+l+1}\}$ with n and l being the number of basis functions and the polynomial order, respectively. If the knots are distributed equidistantly, they are said to be *uniform*. Otherwise, the knots are *non-uniform*. When more than one knot is positioned at the same location, the knots are called *repeated*. In an *open* knot vector, the first and last knots are repeated $l+1$ times, which ensures that the resulting basis functions are interpolatory at the domain boundaries. A non-empty knot interval $[\xi_i \ \xi_{i+1})$ is referred to as *knot span*. For an open uniform knot vector, the number of spans is equal to $n-l$.

The Cox-de Boor formula [25] defines B-spline basis functions recursively, starting with piecewise constants (no repeated knots, i.e. $l=0$):

$$\phi_{i,0}(\xi) = \begin{cases} 1 & \text{if } \xi_i \le \xi < \xi_{i+1}, \\ 0 & \text{otherwise.} \end{cases}$$

For $l > 0$, the basis functions are given by

$$\phi_{i,l}(\xi) = \frac{\xi - \xi_i}{\xi_{i+l} - \xi_i}\phi_{i,l-1}(\xi) + \frac{\xi_{i+l+1} - \xi}{\xi_{i+l+1} - \xi_{i+1}}\phi_{i+1,l-1}(\xi) \qquad \xi \in \Omega.$$

B-spline basis functions satisfy the following properties.

1. They form a partition of unity:

$$\sum_{i=1}^{n} \phi_{i,l}(\xi) = 1 \quad \forall\, \xi.$$

2. Each $\phi_{i,l}$ has compact support $[\xi_i, \xi_{i+l+1}]$.

3. They are non-negative in their support:

$$\phi_{i,l}(\xi) \geq 0 \quad \forall\, \xi.$$

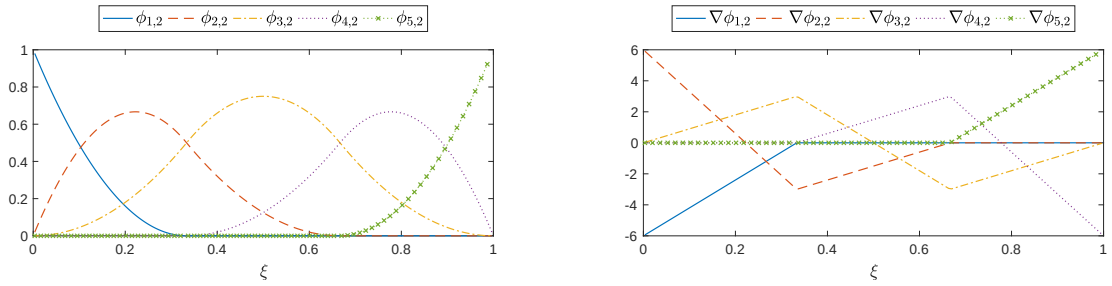

(a) (b)

Figure 2: Example of quadratic B-splines for an open, uniform knot vector (a), gradient of a quadratic B-spline basis function (b).

The gradients of the B-spline basis functions can be defined as follows [25]:

$$\frac{d\phi_{i,l}(\xi)}{d\xi} = \frac{l}{\xi_{i+l} - \xi_i}\phi_{i,l-1}(\xi) - \frac{l}{\xi_{i+l+1} - \xi_{i+1}}\phi_{i+1,l-1}(\xi). \tag{17}$$

In this paper, we only consider open, uniform knot vectors and restrict the analysis to quadratic B-spline basis functions (i.e., $l = 2$). Figure 2 shows quadratic basis functions with $\Xi = \{0, 0, 0, 1/3, 2/3, 1, 1, 1\}$ and the corresponding gradients.

5 Function reconstruction

An important property of MPM, DDMPM, and BSMPM is that they preserve the total mass $\mathcal{M}$ and linear momentum $\mathcal{P}$ of the system. For a one-phase continuum, Equation (14), Equation (16), and the partition of unity property of the basis functions yield:

$$\mathcal{M} = \sum_{i=1}^{N_n} m_i = \sum_{i=1}^{N_n}\sum_{p=1}^{N_p} m_p\phi_i(x_p) = \sum_{p=1}^{N_p} m_p \sum_{i=1}^{N_n} \phi_i(x_p) = \sum_{p=1}^{N_p} m_p,$$

$$\mathcal{P} = \sum_{i=1}^{N_n} m_i v_i = \sum_{i=1}^{N_n} m_i \frac{1}{m_i}\sum_{p=1}^{N_p} m_p\phi_i(x_p)v_p = \sum_{p=1}^{N_p} m_p v_p \sum_{i=1}^{N_n} \phi_i(x_p) = \sum_{p=1}^{N_p} m_p v_p.$$

The time index is dropped to simplify the notation. In a similar way, MPM, DDMPM, and BSMPM conserve the mass and momentum for two-phase formulation.

MPM can be viewed as a version of FEM, where the particles provide data for the background grid. In fact, the scattered material-point information is projected to the grid by reconstructing a function of interest and evaluating it at the nodes. Sulsky and Gong [7, 8] point out that MPM reconstructs functions using a particular case of Shepard interpolation [6] that can introduce significant errors. They improve the accuracy of the method by adopting higher-order reconstruction techniques. In the modified versions, the velocity, density, and stress fields are reconstructed from the particle data and evaluated either at the nodes or element centres. The MPM-integration is then replaced by a one-point quadrature rule. Moreover, Tielen et al. [14, 26] introduce an alternative reconstruction technique for BSMPM. They reconstruct functions using cubic-spline interpolation and integrate with a two-point Gauss rule on the half of each non-zero interval. However, it should be noted that while the adjusted mapping techniques can increase the accuracy of the solution, they do not necessarily conserve the total mass and momentum of the system.

In this section, we introduce an alternative reconstruction technique, called Taylor Least Squares (TLS), that maintains the conservative properties of the standard algorithm. Its fundamental concepts are described in Sections 5.1 – 5.3. The use of the TLS technique for mapping the particle data within the material point methods is outlined in Section 5.4. A mathematical analysis of the conservation properties of the technique is provided in Section 5.5.

5.1 Least Squares approximation

Given a set of N_p distinct data points, $\{x_p\}_{p=1}^{N_p}$, and the data values of these points, $\{u(x_p)\}_{p=1}^{N_p}$, we assume that $u \in F$, where F is a normed function space on $\mathbb{R}$, and $P = \text{span}\{\psi_i\}_{i=1}^{n_b} \subset F$ is a set of n_b basis functions. The Least Squares [15] approximation at a point $x \in \mathbb{R}$ is the value $w^* \in P$ that minimizes, among all $w \in P$, the Least Squares error:

$$E = \sum_{p=1}^{N_p} \left(w(x_p) - u(x_p)\right)^2.$$

Using the basis function vector, $\boldsymbol{\psi}(x) = [\psi_1(x)\ \psi_2(x)\ \ldots\ \psi_{n_b}(x)]^T$, and vector of unknown coefficients, $\mathbf{a} = [a_1\ a_2\ \ldots\ a_{n_b}]^T$, the Least Squares approximation can be written as

$$w^*(x) = \sum_{i=1}^{n_b} a_i \psi_i(x) = \boldsymbol{\psi}^T(x)\mathbf{a}.$$

In order to compute the coefficient vector, $\frac{\partial E}{\partial a_i}$ is set to zero for $i = 1, 2, \ldots, n$, leading to the normal equations:

$$\sum_{p=1}^{N_p} \boldsymbol{\psi}(x_p) \left(\boldsymbol{\psi}^T(x_p)\mathbf{a} - u(x_p)\right) = \mathbf{0}.$$

Therefore, we obtain the following expression:

$$\mathbf{a} = \left(\sum_{p=1}^{N_p} \boldsymbol{\psi}(x_p)\boldsymbol{\psi}^T(x_p)\right)^{-1} \sum_{p=1}^{N_p} \boldsymbol{\psi}(x_p)u(x_p). \tag{18}$$

Defining $D = \sum_{p=1}^{N_p} \boldsymbol{\psi}(x_p)\boldsymbol{\psi}^T(x_p)$, $B = [\boldsymbol{\psi}(x_1)\boldsymbol{\psi}(x_2)\ldots\boldsymbol{\psi}(x_{N_p})]$, and $U = [u(x_1)u(x_2)\ldots u(x_{N_p})]^T$, the Least Squares solution is given by

$$w^*(x) = \boldsymbol{\psi}^T(x)D^{-1}BU. \tag{19}$$

What remains to be specified is the basis for P.

5.2 Taylor basis functions

Available choice that leads to an overall conservative reconstruction scheme are the local Taylor basis functions [16]. To define these basis functions we introduce the concept of the volume average of a function f over cell e:

$$\overline{f} = \frac{1}{|\Omega_e|}\int_{\Omega_e} f\, d\Omega_e,$$

where $|\Omega_e|$ is the volume of cell e. In one dimension, $\Omega_e = [x_{min}, x_{max}]$ with $x_{max} > x_{min}$, and $|\Omega_e| = x_{max} - x_{min}$.

The Taylor basis functions are then given by

$$\begin{aligned}
\psi_1 &= 1,\\
\psi_2 &= \frac{x - x_c}{\Delta x},\\
\psi_3 &= \frac{(x - x_c)^2}{2\Delta x^2} - \frac{\overline{(x - x_c)^2}}{2\Delta x^2},\ \text{etc.}
\end{aligned}$$

Here, $x_c = \frac{x_{max}+x_{min}}{2}$ is the cell centroid x_c of a cell e, and $\Delta x = \frac{x_{max}-x_{min}}{2}$.

An important quality of the Taylor basis that will ensure the conserving property of the reconstruction technique is the following:

$$\int_{\Omega_e} \psi_i\, d\Omega_e = \begin{cases} |\Omega_e| & \text{if } i = 1,\\ 0 & \text{if } i \neq 1. \end{cases} \tag{20}$$

5.3 Taylor Least Squares reconstruction

The TLS approach uses local Taylor basis functions for the Least Squares approximation of a function f:

$$f(x) \approx \hat{f}(x) = \sum_{i=1}^{n_b} a_i \psi_i(x). \tag{21}$$

Suppose that $\int_{\Omega_e} f(x)\, d\Omega_e = c$ with $c \in \mathbb{R}$ required to be conserved by the reconstruction. Then, using Equation (20), we obtain:

$$\int_{\Omega_e} \hat{f}(x)\, d\Omega_e = \int_{\Omega_e} \sum_{i=1}^{n_b} a_i \psi_i(x)\, d\Omega_e = \sum_{i=1}^{n_b} a_i \int_{\Omega_e} \psi_i(x)\, d\Omega_e = a_1 |\Omega_e|. \tag{22}$$

Therefore, the integral is conserved after the reconstruction if

$$a_1 = \frac{c}{|\Omega_e|}. \tag{23}$$

It should be noted that Equation (23) can be enforced explicitly.

We illustrate this property by reconstructing $f(x) = \sin(x) + 2$ on $[0, 4\pi]$. In this case, the integral is equal to 8π. The domain is divided into four elements of size π and contains 11 data points. Two data points are located at the boundaries of the first element, (i.e., 0 and π). In $[2\pi, 3\pi]$, the data points are distributed uniformly in the interior of the domain. The remaining data points have random positions creating different types of data distribution within an element.

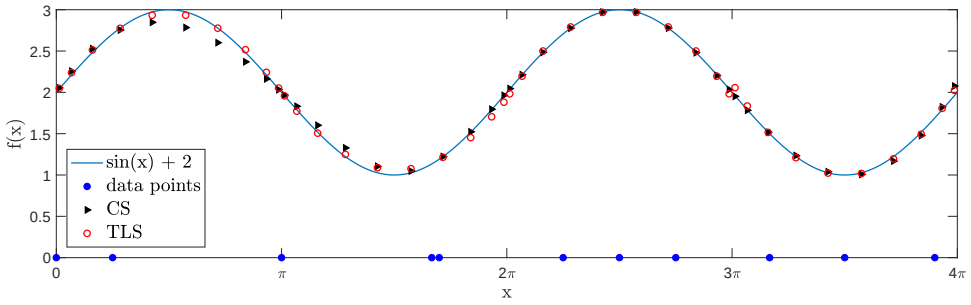

Figure 3: Cubic-spline (CS) and TLS reconstructions of $f(x) = sin(x) + 2$ on $[0, 4\pi]$ for different types of data point distribution within an element.

The TLS approximation is obtained using three Taylor basis functions. We compare its performance with that of the cubic-spline reconstruction in terms of the Root-Mean-Square (RMS) error for function f and the relative error for the integral of f. The RMS error is computed using 100 Gauss points per element, while for the numerical integration, the reconstructed function is evaluated only at two Gauss points within each element. Figure 3 visualises the data point distribution, and the cubic-spline and TLS reconstructions of f for 10 Gauss points per element, while Table 1 provides the corresponding errors.

Table 1: Errors made by TLS and cubic-spline reconstruction for $f(x) = \sin(x) + 2$ and its integral on $[0, 4\pi]$ with four elements and eleven data points.

Error	Cubic-splines	TLS
RMS error for function	$6.0867 \cdot 10^{-2}$	$3.9967 \cdot 10^{-2}$
Relative error for integral	$4.2759 \cdot 10^{-2}$	$2.7903 \cdot 10^{-15}$

Table 1 shows that, for the considered example, the TLS technique outperforms the cubic-spline reconstruction when the conservation and accuracy properties are considered. In fact, the TLS approach preserves the integral up to machine precision. However, Figure 3 shows that the performance of the TLS technique depends on the distribution of the data points within each element.

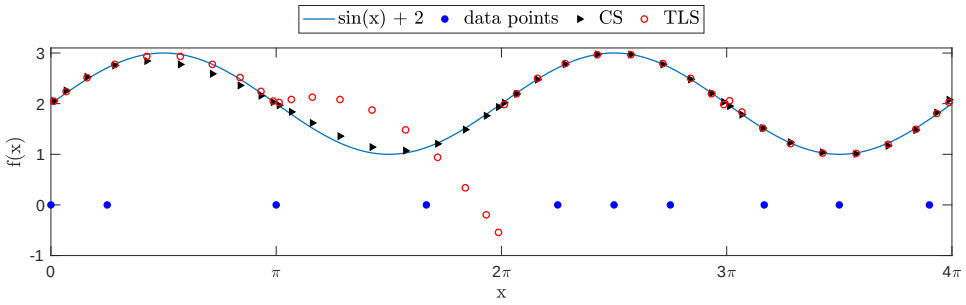

Figure 4: Comparison of cubic-spline and TLS reconstructions of $f(x) = sin(x) + 2$ on $[0, 4\pi]$ for a challenging local data distribution.

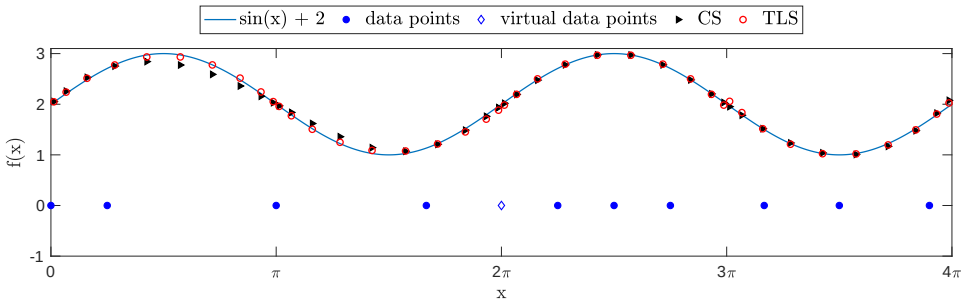

Figure 5: Comparison of cubic-spline and TLS reconstructions of $f(x) = sin(x) + 2$ on $[0, 4\pi]$ with a virtual data point at 2π.

In some rare cases, data distribution can locally decrease the quality of the TLS approximation, but have little influence on cubic-spline interpolation. An example is provided in Figure 4, where $[\pi, 2\pi]$ contains only two data points located at π and $5/3\pi$. This particular data distribution leads to a linear dependence between the columns of matrix D from Equation (19) and, hence, distorts the TLS approximation within $[\pi, 2\pi]$. Therefore,

the condition number of D can be used to detect the data distributions that decrease the accuracy of the TLS technique. In addition, the quality of the TLS technique in such situations can easily be improved.

First of all, the singularity of D can be prevented by reducing the number of basis functions used for the reconstruction on $[\pi, 2\pi]$. While this approach will preserve the conservative properties of the TLS technique and can be implemented in a straightforward manner, it will lower the accuracy of the method. Another option is available to maintain the high quality of the reconstruction. In this approach, the TLS approximation of f for $[2\pi, 3\pi]$ is evaluated at 2π, the obtained value is then used for the function reconstruction on $[\pi, 2\pi]$, but is excluded from the computation of a_1 in Equation (23). We refer to 2π as a *virtual* data point, because its value is produced by the application of the TLS technique to one cell in order to enlarge the set of data points, upon which the least squares approximation is based, in a different cell. Moreover, virtual points do not influence the conservative properties of the technique. Figure 5 illustrates the approximation improved by including a virtual data point at 2π.

5.4 Mapping of particle data

When the TLS reconstruction is considered as part of a material point method, particles serve as data points. To conserve the integral of a certain quantity within each element, the coefficient of the first basis function is specified according to Equation (23). The remaining coefficients are calculated from Equation (18) without ψ_1 thereby not changing the integral value. When the conservation is not required, a standard least-square approach is followed. This implies that all unknown coefficients are obtained from the least-square approximation.

A TLS reconstruction is applied to replace the MPM-integration in Equations (15) and (16), and their equivalents for a two-phase material by an exact method, such as an element-wise Gauss quadrature. The internal forces at the DOFs are computed as follows:

1. Apply a quadratic TLS approach to reconstruct the stress field from the particle data within each active element without specifying the coefficient of the first Taylor basis function:

$$\hat{\sigma}_e = \sum_{i=1}^{n_b} s_i \psi_i, \tag{24}$$

   where s_i is the coefficient corresponding to Taylor basis function i. Outside of element e, $\hat{\sigma}_e$ is zero. The global approximation of the density function, $\hat{\sigma}$, is then equal to

$$\hat{\sigma} = \sum_{e=1}^{N_e} \hat{\sigma}_e.$$

2. Integrate the stress approximation using a two-point Gauss quadrature:

$$\mathbf{f}^{\text{int}} \approx \int_\Omega \hat{\sigma}(x,t) \nabla \boldsymbol{\phi} \, d\Omega = \sum_{g=1}^{N_g} \hat{\sigma}\left(x_g\right) \nabla \boldsymbol{\phi}\left(x_g\right) \omega_g,$$

where N_g is the total number of Gauss points, x_g is the global position of a Gauss point, and ω_g is the weight of a Gauss point. To assure the exact integration of the approximated function N_g should be selected so that $n_b \leq \frac{2N_g}{N_e}$.

The material-point velocities are mapped to the DOFs in the following manner:

1. Apply a quadratic TLS approach to reconstruct the density field and the product of density and velocity from the particle data within each active element, while preserving the mass and momentum of the element:

$$\hat{\rho}_e = \sum_{i=1}^{n_b} r_i \psi_i \text{ with } r_1 = \frac{1}{|\Omega_e|} \sum_{\{p|x_p \in \Omega_e\}} m_p$$
$$(\widehat{\rho v})_e = \sum_{i=1}^{n_b} \gamma_i \psi_i \text{ with } \gamma_1 = \frac{1}{|\Omega_e|} \sum_{\{p|x_p \in \Omega_e\}} m_p v_p.$$

   where r_i and γ_i are the coefficients corresponding to Taylor basis function i. Outside of element e, $\hat{\rho}_e$ and $(\widehat{\rho v})_e$ are zero. The global approximations are then equal to

$$\hat{\rho} = \sum_{e=1}^{N_e} \hat{\rho}_e \text{ and } (\widehat{\rho v}) = \sum_{e=1}^{N_e} (\widehat{\rho v})_e.$$

2. Integrate the approximations using a two-point Gauss quadrature to obtain the momentum vector $\mathbf{p}$ and and the consistent mass matrix M^C:

$$\mathbf{p} = \sum_{g=1}^{N_g} \hat{\rho}(x_g) \omega_g \boldsymbol{\phi}(x_g) \hat{v}(x_g), \tag{25}$$

$$M^C = \sum_{g=1}^{N_g} \hat{\rho}(x_g) \omega_g \boldsymbol{\phi}(x_g) (\boldsymbol{\phi}(x_g))^T, \tag{26}$$

3. Compute the velocity vector:

$$\mathbf{v} = (M^C)^{-1} \mathbf{p}. \tag{27}$$

   It should be noted that M^C may be replaced by a lumped mass matrix without a loss of conservative properties of the algorithm.

We obtain the approximations with a quadratic TLS reconstruction. This implies that only the first three Taylor basis functions are used (i.e, $n_b = 3$). In this case, a two-point Gauss rule within each element leads to an exact integration. For a two-phase computation, the TLS approach is additionally applied to compute the internal force and velocity of the liquid phase. Furthermore, from Section 5.3 it follows that optimal performance of the TLS technique requires at least three particles in each element at the beginning of the simulation. Since this particle distribution is not preserved under large deformations, virtual data points may be used to improve the accuracy of the approximation within elements that contain only one or two material-points.

5.5 Conservation of mass and momentum

As mentioned in Section 5.4, the TLS technique reconstructs the density field and the product of density and velocity inside each element in the following way:

$$\rho_e \approx \hat{\rho}_e = \sum_{i=1}^{n_b} r_i \psi_i \qquad \text{with } r_1 = \frac{1}{|\Omega_e|} \sum_{\{p|x_p \in \Omega_e\}} m_p$$

$$(\rho v)_e \approx (\widehat{\rho v})_e = \sum_{i=1}^{n_b} \gamma_i \psi_i \text{ with } \gamma_1 = \frac{1}{|\Omega_e|} \sum_{\{p|x_p \in \Omega_e\}} m_p v_p,$$

According to Equation (22) and (23), this preserves the mass $\mathcal{M}_e$ and momentum $\mathcal{P}_e$ of element e. As a result, the total mass and momentum of the system are conserved after the TLS reconstruction:

$$\mathcal{M} = \sum_{e=1}^{N_e} \mathcal{M}_e = \sum_{e=1}^{N_e} \sum_{\{p|x_p \in \Omega_e\}} m_p = \sum_{p=1}^{N_p} m_p, \tag{28}$$

$$\mathcal{P} = \sum_{e=1}^{N_e} \mathcal{P}_e = \sum_{e=1}^{N_e} \sum_{\{p|x_p \in \Omega_e\}} m_p v_p = \sum_{p=1}^{N_p} m_p v_p. \tag{29}$$

The mass- and momentum- conservative properties of the mapping obtained using TLS reconstruction and Gauss quadrature can be shown as well.

Since the total mass is equal to the sum of the entries in the consistent mass matrix from Equation (26), it can be written as

$$\begin{aligned} \mathcal{M} &= \sum_{i=1}^{N_n} \sum_{j=1}^{N_n} M_{ij}^C = \sum_{i=1}^{N_n} \sum_{j=1}^{N_n} \sum_{g=1}^{N_g} \hat{\rho}\left(x_g\right) \omega_g \phi_i\left(x_g\right) \phi_j\left(x_g\right) \\ &= \sum_{g=1}^{N_g} \hat{\rho}\left(x_g\right) \omega_g \sum_{i=1}^{N_n} \phi_i\left(x_g\right) \sum_{j=1}^{N_n} \phi_j\left(x_g\right) = \sum_{g=1}^{N_g} \hat{\rho}\left(x_g\right) \omega_g. \end{aligned} \tag{30}$$

The last equality is derived using the partition of unity property of piecewise-linear and B-spline basis functions. In the remaining part of the proof, we assume that $n_b \leq \frac{2N_g}{N_e}$, so that the Gauss quadrature with $\frac{N_g}{N_e}$ integration points per element (or knot span) is exact. Therefore, the following holds:

$$\mathcal{M} = \sum_{g=1}^{N_g} \hat{\rho}\left(x_g\right) \omega_g = \sum_{e=1}^{N_e} \sum_{\{g|x_g \in \Omega_e\}} \hat{\rho}_e\left(x_g\right) \omega_g = \sum_{e=1}^{N_e} \int_{\Omega_e} \hat{\rho}_e \, d\Omega_e = \sum_{e=1}^{N_e} \mathcal{M}_e = \sum_{p=1}^{N_p} m_p.$$

The last two steps emerge from the conservation of mass per element and Equation (28).

For the linear momentum, we also assume that $n_b \leq \frac{2N_g}{N_e}$. Following the above steps, the total momentum after the mapping can be written as

$$\begin{aligned}\mathcal{P} &= \sum_{i=1}^{N_n} p_i = \sum_{i=1}^{N_n}\sum_{g=1}^{N_g}(\widehat{\rho v})(x_g)\omega_g\phi_i(x_g) = \sum_{g=1}^{N_g}(\widehat{\rho v})(x_g)\omega_g\sum_{i=1}^{N_n}\phi_i(x_g)\\ &= \sum_{g=1}^{N_g}(\widehat{\rho v})(x_g)\omega_g = \sum_{e=1}^{N_e}\sum_{\{g|x_g\in\Omega_e\}}(\widehat{\rho v})_e(x_g)\omega_g\\ &= \sum_{e=1}^{N_e}\int_{\Omega_e}(\widehat{\rho v})_e d\Omega_e = \sum_{e=1}^{N_e}\mathcal{P}_e = \sum_{p=1}^{N_p} m_p v_p.\end{aligned}$$

Therefore, we have shown that if the Gauss quadrature is performed using a sufficient number of integration points, the mass and momentum balance is satisfied not only by the TLS function reconstruction, but also by its combination with the Gauss quadrature.

6 Numerical results

For the spatial convergence analyses, we minimise the contribution of temporal errors by using small time-step sizes and short simulation times. The material-point solutions are considered at the particle positions, which implies that the one-phase examples are studied in terms of the particle displacement, velocity, and stress. For two-phase problems, we look at the displacement of the solid phase, velocities of both phases, effective stress, and pore pressure.

We study the conservative properties of the material point methods by calculating the maximum relative errors in the total mass and momentum over all time steps before and after the computation of the velocity at the DOFs. For MPM, DDMPM, and BSMPM, the errors in the mass and momentum are bounded by 10^{-15} for the vibrating bar benchmark, and 10^{-13} for the consolidation example. Therefore, the TLS results are only compared to those obtained with the cubic-spline reconstruction.

6.1 Vibrating bar

This example describes the vibration of a one-phase bar with fixed ends. The motion triggered by an initial velocity that varies along the bar is captured by Equations (1) - (4) with $g = 0$ (i.e., the gravitational force is neglected) and the following initial and boundary conditions:

$$\begin{aligned}&u(x,0) = 0, \quad v(x,0) = v_0 \sin\left(\frac{\pi x}{2H}\right), \quad \sigma(x,0) = 0;\\ &u(0,t) = 0, \quad u(H,t) = 0.\end{aligned}$$

For small strains, the analytical solution in terms of displacement, velocity, and stress is given by

$$u(x,t) = \frac{v_0 H}{\pi\sqrt{E/\rho}} \sin\left(\frac{\pi\sqrt{E/\rho}\,t}{H}\right) \sin\left(\frac{\pi x}{H}\right),$$
$$v(x,t) = v_0 \cos\left(\frac{\pi\sqrt{E/\rho}\,t}{H}\right) \sin\left(\frac{\pi x}{H}\right),$$
$$\sigma(x,t) = v_0\sqrt{E\rho} \sin\left(\frac{\pi\sqrt{E/\rho}\,t}{H}\right) \cos\left(\frac{\pi x}{H}\right).$$

Table 2 provides exemplary parameter values for the vibrating bar benchmark under small deformations. The time-step size and total simulation time are $1 \cdot 10^{-7}$ s and $1.9 \cdot 10^{-6}$ s, respectively. Furthermore, the number of elements (knot spans) is varied from 5 to 40, while the number of particles per cell (PPC) is fixed to 12. Grid crossing does not occur, and the maximal observed strain is equal to $5.3 \cdot 10^{-7}$ m.

Table 2: Exemplary parameters allowing for small deformations in the vibrating bar problem.

Parameter	Symbol	Value	Unit
Height	H	1.00	m
Density	ρ	$2.00 \cdot 10^3$	kg/m^3
Young's modulus	E	$7.00 \cdot 10^6$	Pa
Max. initial velocity	v_0	0.28	m/s^2

The results in terms of spatial errors are shown in Figure 6. As expected, MPM with piecewise-linear basis functions demonstrates second-order convergence in both the displacement and velocity. Since the stress is not discretised, its convergence rate is one. The application of the TLS reconstruction technique, as well as the cubic-spline interpolation, has almost no influence on the stress, but decreases the displacement error by a factor of 1.7. For DDMPM, the application of the reconstruction techniques tends to reduce not only the error in the displacement, but also in the stress. However, other results are similar to those obtained for MPM.

The use of quadratic B-splines as basis functions leads to a significant decrease in the error and a higher order of convergence for the velocity, but causes problems at the boundaries of the domain for both stress and displacement. The absolute error in stress over the domain is shown in Figure 7. The large values of the error at the boundaries prevent the reduction of the RMS error and worsen the convergence properties of the method. However, the use of BSMPM with the function reconstruction techniques eliminates the boundary issues. An example is provided in Figure 8. Consequently, third-order convergence is obtained for all the considered quantities. It should also be noted that the integration of

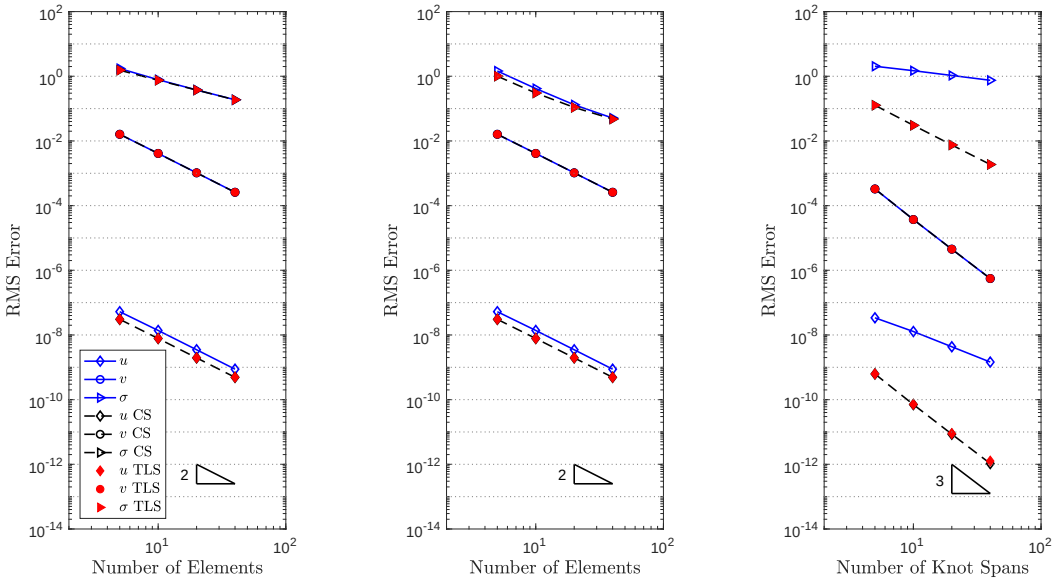

(a) MPM (b) DDMPM (c) BSMPM

Figure 6: Spatial convergence of material point methods for the vibrating bar problem without grid crossing. The results are shown for the material point methods without reconstruction techniques (solid blue line, empty marker); with cubic-spline reconstruction, CS, (dashed black line, empty marker); and with TLS reconstruction (red filled marker).

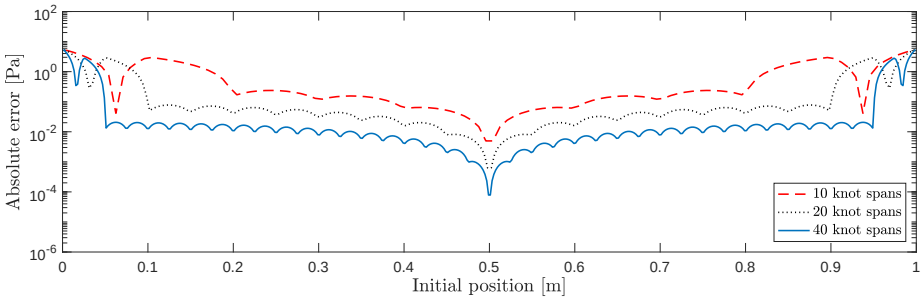

Figure 7: Absolute error obtained with BSMPM for stress distribution in the vibrating bar problem without grid crossing.

the TLS or spline reconstruction in BSMPM produces more accurate results than the other considered methods.

Table 3 compares the relative error in mass and momentum made using the TLS and cubic-spline reconstructions. The results are provided for MPM, DDMPM, and BSMPM applied to the vibrating bar problem discretised by 40 elements (knot spans) and 12 PPC. They demonstrate that while the cubic-spline interpolation tends to accurately conserve the mass, it produces errors of order 10^{-6} for the linear momentum. The errors produced

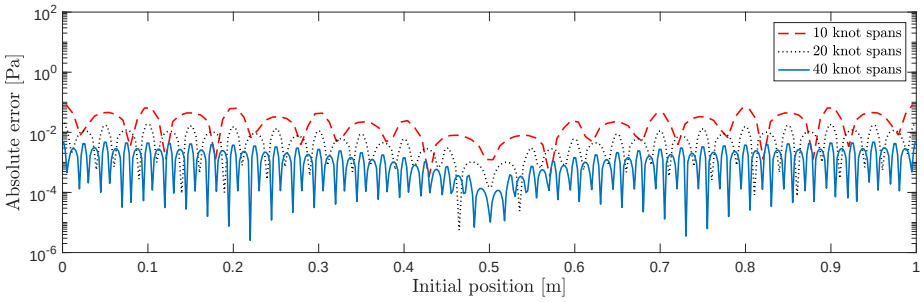

Figure 8: Absolute error obtained with BSMPM-TLS for stress distribution in the vibrating bar problem without grid crossing.

Table 3: Maximum relative errors in the total mass $\mathcal{M}$ and momentum $\mathcal{P}$ over the simulation run with cubic-spline (CS) and TLS reconstructions when grid crossing does not occur. The vibrating bar is discretised using 40 elements (knot spans) and 12 PPC.

	MPM		DDMPM		BSMPM	
	$\text{Error}_{\mathcal{M}}$	$\text{Error}_{\mathcal{P}}$	$\text{Error}_{\mathcal{M}}$	$\text{Error}_{\mathcal{P}}$	$\text{Error}_{\mathcal{M}}$	$\text{Error}_{\mathcal{P}}$
CS	$2.3825 \cdot 10^{-12}$	$3.7053 \cdot 10^{-6}$	$3.9211 \cdot 10^{-13}$	$3.7053 \cdot 10^{-6}$	$2.3825 \cdot 10^{-12}$	$3.7053 \cdot 10^{-6}$
TLS	$7.5033 \cdot 10^{-15}$	$2.1007 \cdot 10^{-16}$	$7.3896 \cdot 10^{-15}$	$2.5208 \cdot 10^{-16}$	$7.5033 \cdot 10^{-15}$	$2.1007 \cdot 10^{-16}$

by the TLS approach consistently remain close to machine precision and, hence, are orders of magnitude smaller than those generated by the cubic-spline interpolation.

Table 4: Exemplary parameters allowing for large deformations in the vibrating bar problem.

Parameter	Symbol	Value	Unit
Height	H	1.00	m
Density	ρ	$2.00 \cdot 10^3$	kg/m^3
Young's modulus	E	$4.00 \cdot 10^4$	Pa
Max. initial velocity	v_0	0.80	m/s^2

For large-deformation simulations, the parameters from Table 4 are used. The time-step size and the simulation time are increased to $1 \cdot 10^{-5}$ s and 0.1 s, respectively. The domain is discretised using 20 elements (knot spans) with initially 8 PPC. The maximal strain that is reached is 0.056 m. Since the analytical solution is not available when the vibrating bar experiences large deformations, the numerical results are compared to the solution obtained with the Updated Lagrangian Finite Element Method (ULFEM) [27].

In the standard MPM simulation, material points cross the element boundaries more than 450 times leading to significant inaccuracies in the results. Although grid crossing influences the computation of the displacement and velocity, its most evident consequences are in the stress distribution. DDMPM and BSMPM reduce the grid-crossing error, but their results still significantly deviate from the solution provided by ULFEM. This is shown

in Figure 9. The figure also illustrates that the application of the TLS approximation

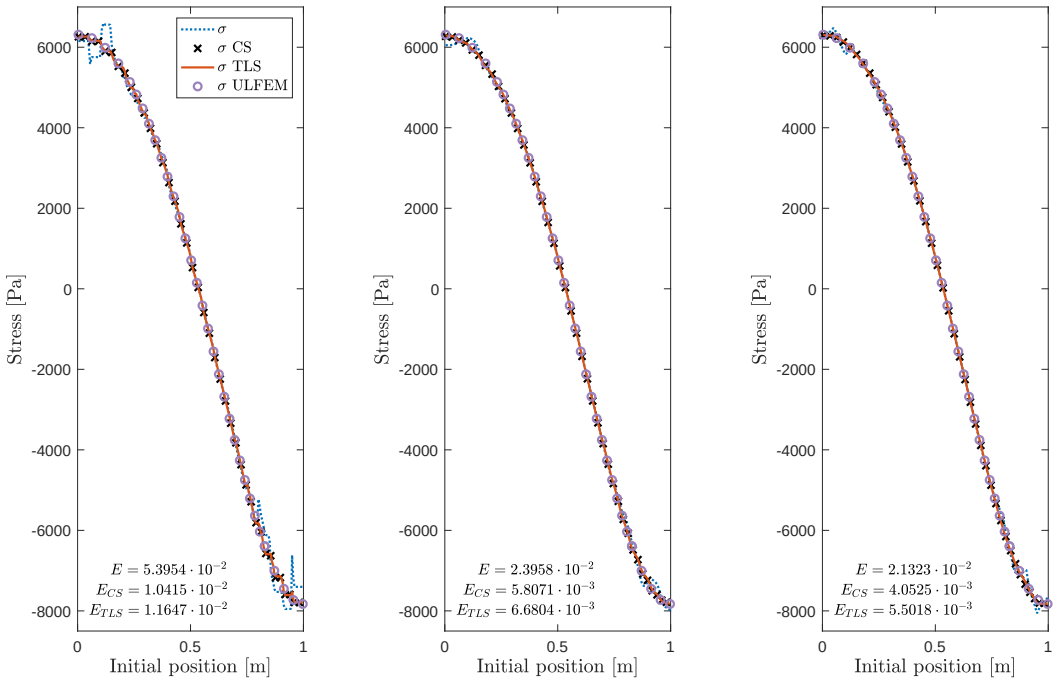

(a) MPM (b) DDMPM (c) BSMPM

Figure 9: Stress distribution and corresponding relative errors in the L_2-norm in the vibrating bar problem with grid crossing. The results are obtained for the material point methods without reconstruction technique (dotted blue line); with cubic-spline reconstruction, CS (black cross marker); with TLS reconstruction (solid red line); and ULFEM (grey circle marker).

Table 5: Maximum relative errors in the total mass $\mathcal{M}$ and momentum $\mathcal{P}$ over the simulation run with cubic-spline (CS) and TLS reconstructions when grid crossing occurs. The vibrating bar is discretised using 40 elements (knot spans) and 12 PPC.

	MPM		DDMPM		BSMPM	
	$\text{Error}_{\mathcal{M}}$	$\text{Error}_{\mathcal{P}}$	$\text{Error}_{\mathcal{M}}$	$\text{Error}_{\mathcal{P}}$	$\text{Error}_{\mathcal{M}}$	$\text{Error}_{\mathcal{P}}$
CS	$8.2017 \cdot 10^{-5}$	$7.9819 \cdot 10^{-5}$	$3.5971 \cdot 10^{-5}$	$3.7506 \cdot 10^{-5}$	$7.4131 \cdot 10^{-7}$	$1.5794 \cdot 10^{-5}$
TLS	$2.9331 \cdot 10^{-14}$	$5.8469 \cdot 10^{-15}$	$2.9104 \cdot 10^{-14}$	$5.7725 \cdot 10^{-15}$	$2.9104 \cdot 10^{-14}$	$5.7205 \cdot 10^{-15}$

or the cubic-spline reconstruction leads to close agreement of the MPM, DDMPM, and BSMPM solutions with that of ULFEM. The maximal reduction of the relative error in L_2-norm made by standard MPM is achieved when the reconstruction techniques are combined with BSMPM. More precisely, the integration of the spline interpolation or the

TLS reconstruction in BSMPM decreases the MPM error by a factor of 13.3 and 9.8, respectively. On the other hand, the conjunction of the reconstruction techniques with DDMPM leads to highly accurate results as well. The spline and TLS reconstruction reduces the MPM error by a factor of 9.3 and 8.1, respectively. As expected, the TLS approximation conserves the total mass and linear momentum significantly more accurately than the spline interpolation, regardless of the material-point method. The conservative properties of the reconstruction techniques are provided in Table 5.

6.2 Consolidation

In this example from AL-Kafaji [24], we consider a column of height H that consists of fully saturated soil and has an impermeable bottom. On the top surface, a constant load q is applied. Initially, the load is carried by the liquid phase maximising the pore pressure. After water starts to drain out, the load is gradually transferred to the solid phase, and the excess pore pressure starts to decrease. In the final stage, the water drainage no longer occurs and the load is fully shifted to the solid phase. The consolidation process is described by Equations (5) - (9) with $g = 0$ and $\partial\sigma/\partial x = 0$ (i.e., the gravity is neglected and the total stress is constant). The boundary and initial conditions are:

$$\begin{aligned} &u_s(x,0) = 0, \quad v_s(x,0) = 0, \quad \sigma(x,0) = q, \quad v_w(x,0) = 0, \quad p\,(x,0) = q, \\ &u_s(0,t) = 0, \quad \sigma(H,t) = q, \quad v_w(0,t) = 0, \quad p\,(H,t) = 0. \end{aligned}$$

It should be noted that the boundary and initial conditions for this case study are incompatible. According to the boundary conditions $p\,(H,0) = 0$, while the initial conditions state that $p\,(H,0) \neq 0$.

The analytical solution for the pore pressure is given by [28]:

$$p\,(x,t) = \frac{4p_0}{\pi} \sum_{j=1}^{\infty} \frac{(-1)^{j-1}}{2j-1} \cos\left((2j-1)\frac{\pi x}{2H}\right) \exp\left(-(2j-1)^2 \frac{\pi^2 c_v t}{4H^2}\right),$$

where c_v is the consolidation coefficient defined as

$$c_v = \frac{k}{\rho_w g\,(1/E^c + n/K_w)}.$$

This implies that the effective stress, the displacement of the solid phase, and the velocities

of solid and liquid phases are obtained as follows:

$$\sigma'(x,t) = q - \frac{4p_0}{\pi}\sum_{j=1}^{\infty}\frac{(-1)^{j-1}}{2j-1}\cos\left((2j-1)\frac{\pi x}{2H}\right)\exp\left(-(2j-1)^2\frac{\pi^2 c_v t}{4H^2}\right),$$

$$u_s(x,t) = \frac{qx}{E^c} - \frac{8p_0 H}{E^c\pi^2}\sum_{j=1}^{\infty}\frac{(-1)^{j-1}}{(2j-1)^2}\sin\left((2j-1)\frac{\pi x}{2H}\right)\exp\left(-(2j-1)^2\frac{\pi^2 c_v t}{4H^2}\right),$$

$$v_s(x,t) = \frac{2p_0 c_v}{E^c H}\sum_{j=1}^{\infty}(-1)^{j-1}\sin\left((2j-1)\frac{\pi x}{2H}\right)\exp\left(-(2j-1)^2\frac{\pi^2 c_v t}{4H^2}\right),$$

$$v_w(x,t) = -\frac{2p_0 c_v}{H}\left(\frac{1}{K_w} + \frac{1-n}{nE_c}\right)\sum_{j=1}^{\infty}(-1)^{j-1}\sin\left((2j-1)\frac{\pi x}{2H}\right)\exp\left(-(2j-1)^2\frac{\pi^2 c_v t}{4H^2}\right).$$

The first 100,000 terms of the Fourier series are used to ensure the accuracy of the solution.

The exemplary parameters used to simulate the soil consolidation are provided in Table 6. The number of elements (knot spans) varies from 20 to 160, whereas each element (knot span) contains four material points. Moreover, the time-step size and total simulation time are $1 \cdot 10^{-10}$ s and $2 \cdot 10^{-9}$ s. The computation starts at 5 s, because at 0 s the boundary and initial conditions are incompatible, and for $t \in (0, 5\,\mathrm{s})$ the quantities of interest vary quite severely over the domain. For the described settings, the displacement of the material points is bounded by $2.6 \cdot 10^{-4}$ m and grid crossing does not occur.

Table 6: Exemplary parameters allowing for small deformations in the soil consolidation problem.

Parameter	Symbol	Value	Unit
Height	H	1.00	m
Porosity	n	0.40	-
Density liquid phase	ρ_w	$1.00 \cdot 10^3$	kg/m^3
Density solid phase	ρ_s	$2.60 \cdot 10^3$	kg/m^3
Constrained modulus	E^c	$1.00 \cdot 10^7$	Pa
Bulk modulus liquid phase	K_w	$3.00 \cdot 10^8$	Pa
Hydraulic permeability	k	$1.00 \cdot 10^{-5}$	m/s
Total load	q	$-1.00 \cdot 10^4$	Pa

The convergence results for the displacement of the solid phase, velocity of the liquid phase, and pore pressure are provided in Figure 10. The RMS errors of the velocity of the solid phase and the effective stress are not provided, because they show similar behaviour to the corresponding quantities of the solid phase. In contrast to the vibrating bar problem, for this example, MPM shows second-order convergence for all considered quantities. Application of the function reconstruction techniques has no influence on the MPM results.

DDMPM preserves the RMS errors of the displacement, stress, and pore pressure produced by MPM, but as illustrated in Figure 11 it shows a lack of convergence for the

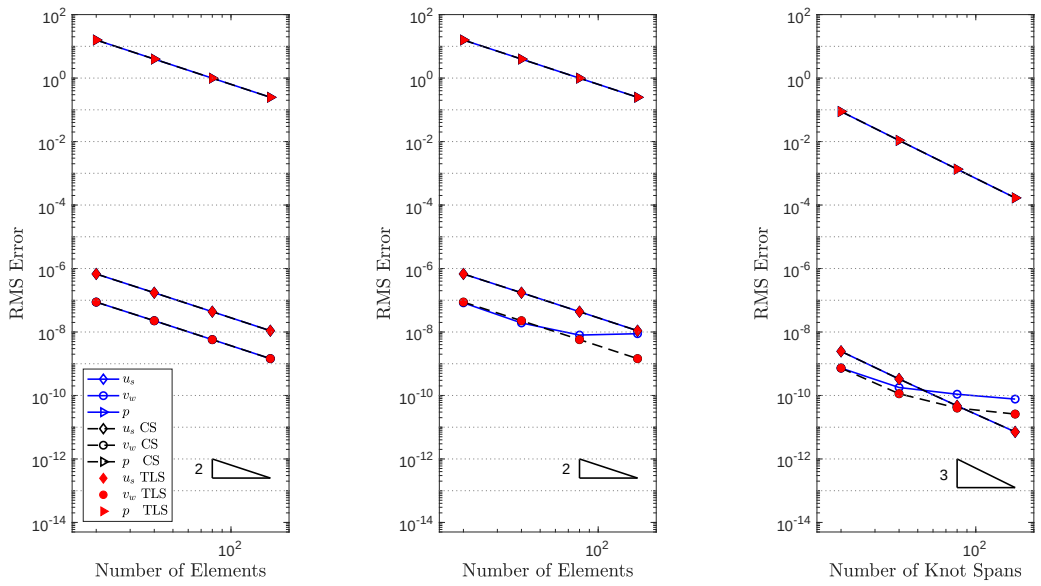

(a) MPM (b) DDMPM (c) BSMPM

Figure 10: Spatial convergence of material point methods for the soil consolidation problem without grid crossing. The results are shown for the material point methods without reconstruction techniques (solid blue line, empty marker); with cubic-spline reconstruction, CS, (dashed black line, empty marker); and with TLS reconstruction (red filled marker).

velocities. The cubic-spline interpolation and TLS reconstruction enable second-order convergence for the velocities and decrease the error for relatively fine grids. This is depicted in Figure 12 for the TLS approach.

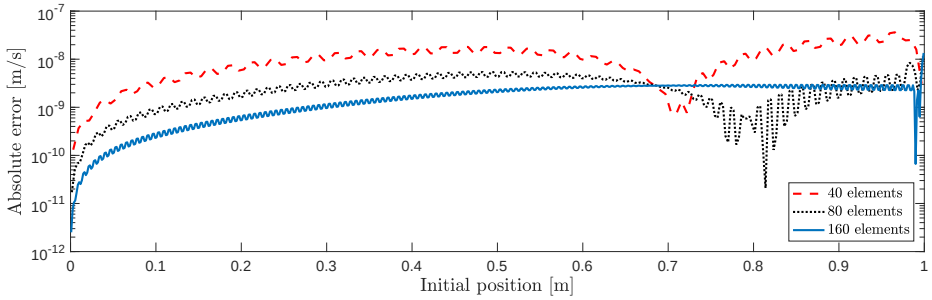

Figure 11: Absolute error obtained with DDMPM for the velocity of the solid phase during soil consolidation without grid crossing.

Furthermore, from Figure 10 it follows that the use of B-spline basis functions considerably reduces the error produced by MPM and DDMPM, and leads to third-order convergence for the displacement, stress and pore pressure. For the velocities, the conver-

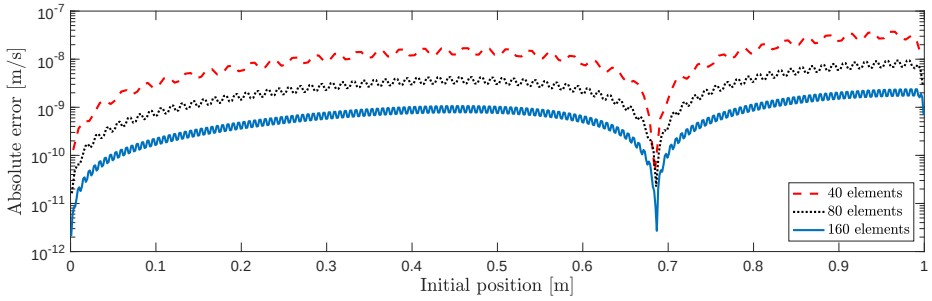

Figure 12: Absolute error obtained with DDMPM-TLS for the velocity of the solid phase during soil consolidation without grid crossing.

gence of BSMPM is hindered at the boundaries of the domain. Although the TLS and spline reconstructions further lower the RMS errors in the velocity, they do not resolve the issues at the boundaries.

In general, the spline interpolation and the TLS technique reconstruct the quantities of interest equally accurately during the simulation of the consolidation process (i.e., the differences in their RMS errors are negligible). In addition, for the cubic-spline interpolation, the relative error in mass of both phases remains at machine precision, but the relative error in momenta varies between $1 \cdot 10^{-9}$ and $2 \cdot 10^{-6}$. The TLS technique conserves the total mass and momentum of the solid and liquid phase at machine precision regardless of the utilised variant of the material point method.

To compel the material points to travel from one cell to another during the consolidation process, the parameters from Table 7 are used. In addition, the computational time is increased to 0.4 s. At the end of the simulation, the total displacement reaches $5.4 \cdot 10^{-2}$ m at the top of the column. The domain is discretised by 120 elements and each element contains 16 material points. Under large deformations, the analytical solutions for the quantities of interest are provided by Xie and Leo [29]. As before, the solution is computed using the first 100,000 terms of the Fourier series.

Table 7: Exemplary parameters allowing for large deformations in the soil consolidation problem.

Parameter	Symbol	Value	Unit
Height	H	1.00	m
Porosity	n	0.40	-
Density liquid phase	ρ_w	$1.00 \cdot 10^3$	kg/m^3
Density solid phase	ρ_s	$2.60 \cdot 10^3$	kg/m^3
Constrained modulus	E^c	$1.00 \cdot 10^6$	Pa
Bulk modulus liquid phase	K_w	$3.00 \cdot 10^7$	Pa
Hydraulic permeability	k	$1.00 \cdot 10^{-5}$	m/s
Total load	q	$-5.00 \cdot 10^5$	Pa

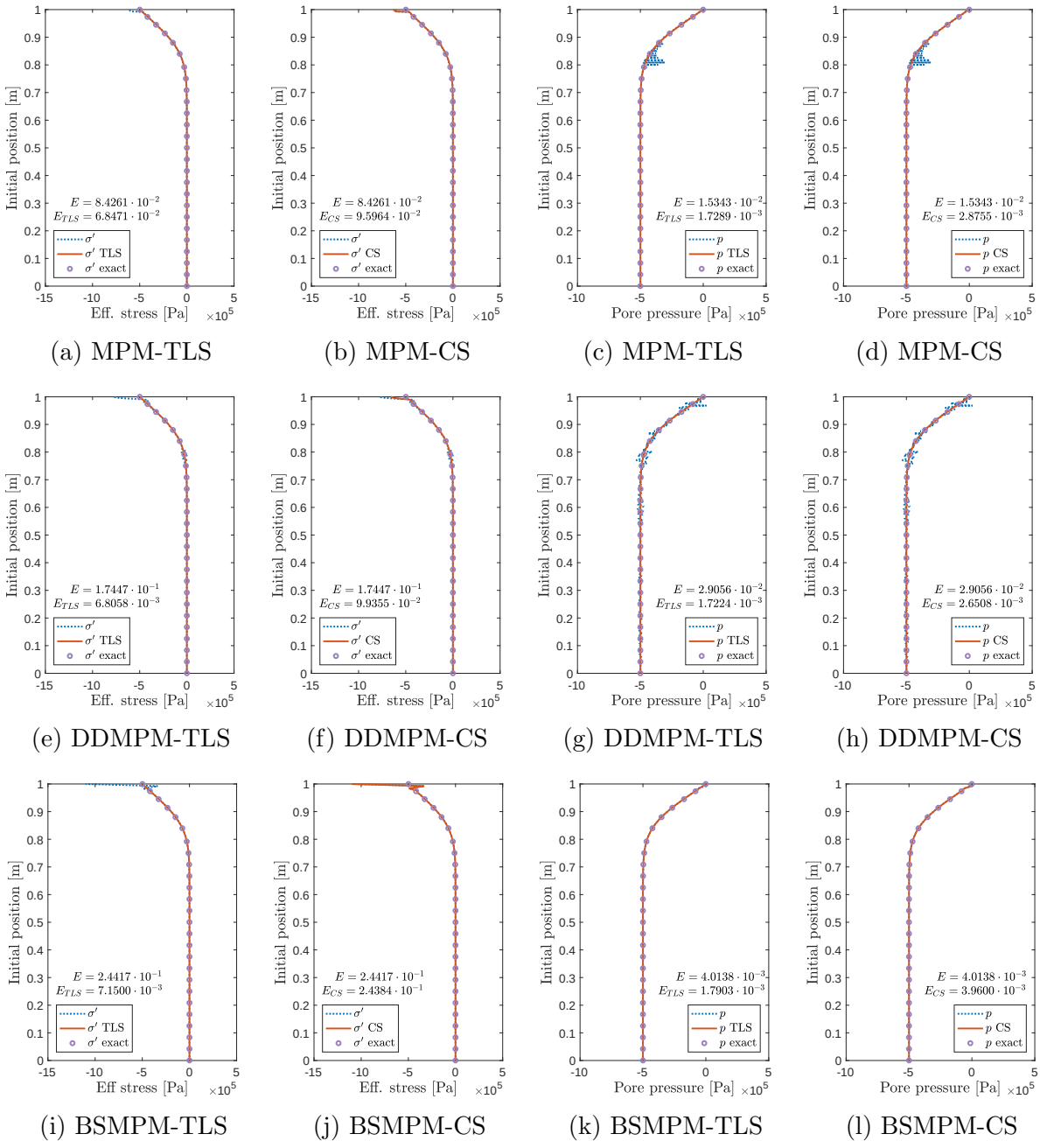

(a) MPM-TLS (b) MPM-CS (c) MPM-TLS (d) MPM-CS

(e) DDMPM-TLS (f) DDMPM-CS (g) DDMPM-TLS (h) DDMPM-CS

(i) BSMPM-TLS (j) BSMPM-CS (k) BSMPM-TLS (l) BSMPM-CS

Figure 13: Comparison of TLS and cubic-spline (CS) reconstructions and the corresponding relative errors in the L_2-norm for consolidation problem with grid crossing. The results are shown for the material point methods without reconstruction techniques (dotted blue line, empty marker); with reconstruction (solid red line, empty marker); and the exact solution (grey circle marker).

Figure 13 provides the results in terms of the effective stress and pore pressure obtained for MPM, DDMPM, and BSMPM, with and without the reconstruction techniques. For the results of BSMPM combined with the TLS technique, the consistent mass matrix in the velocity computation described by Equation (27), is replaced by a lumped mass matrix. This is required to prevent stability issues.

The effect of grid crossing on the MPM solution is clearly illustrated by the pore pressure distribution depicted in Figure 13c and Figure 13d . When the magnitude of the pore pressure starts to decrease, particles move between the elements leading to the oscillations in the solution. This is readily visible for material points originally located between 0.8 m and 0.9 m. The grid crossing effect is present in the velocities as well, but is not observed in the results for the displacement. Since the MPM solution for the effective stress is computed based on the strains, it is also barely influenced by grid crossing. However, the effective stress distribution shows that the method does not satisfy the boundary condition for the total stress at the top surface of the soil column.

Replacing MPM by DDMPM increases the number of oscillations along the column hight and worsens the results at the top boundary. The use of B-splines leads to close agreement with the analytical solution for the pore pressure: it decreases the relative error in the pore water pressure by a factor of 3.8 compared to MPM. However, BSMPM solution deviates from the analytical solution in the effective stress at the top boundary.

In addition, Figure 13 shows that the application of the spline reconstruction technique reduces the grid crossing errors, but the material point methods still fail to satisfy the boundary conditions in terms of the effective stress. However, the technique brings the DDMPM solution for the effective stress at the boundary closer to the values obtained analytically. The TLS reconstruction outperforms the spline interpolation, because it eliminates the unphysical oscillations and ensures that the the boundary conditions are satisfied regardless of the material point method. Finally, the TLS approach preserves the relative errors in total mass and momentum of solid and liquid phase under $4 \cdot 10^{-12}$, while for the cubic-spline reconstruction, the errors reach $1.4 \cdot 10^{-4}$.

7 Summary and conclusions

In this paper, we have introduced Taylor Least Squares reconstruction for material point methods. The proposed technique combines the least squares approximation with local Taylor basis functions to accurately reconstruct the quantities of interest (e.g., stress and density fields) from scattered particle data within each element. We have shown that in contrast to standard reconstruction techniques, the TLS approximation conserves the mass and linear momentum of the system after the material-point data is mapped to the integration points. More importantly, in conjunction with a sufficiently accurate numerical quadrature method, the technique preserves the total mass and momentum after the information is projected to the degrees of freedom of the grid. This implies that the TLS reconstruction maintains the physical properties of the standard material point methods.

For several examples, the TLS technique was applied to MPM, DDMPM, and BSMPM.

Without grid crossing, the reconstruction technique had little influence on MPM, but was able to improve the convergence properties of DDMPM and BSMPM. When material points started to cross cell boundaries, the TLS approximation smoothened the solutions obtained by all considered material point methods for the vibrating bar problem and brought them closer to the solution computed by ULFEM. For the consolidation problem, the proposed technique substantially decreased the unphysical oscillations in the results computed by MPM, DDMPM, and BSMPM, and ensured that they satisfied the boundary conditions in terms of the effective stress. Furthermore, the TLS technique was also compared to a spline reconstruction technique. In general, the differences in spatial accuracy of the reconstruction approaches were negligible, but the error in total mass and linear momentum was consistently much lower for the TLS reconstruction. In contrast to the TLS function reconstruction, the cubic-spline reconstruction technique was not able to follow the analytical solution for the effective stress at the loaded boundary during the simulations of the consolidation process. Therefore, this study has demonstrated that the integration of the TLS technique into the material point methods leads to a higher accuracy of the material point methods without losing their fundamental physical properties.

8 Acknowledgments

This research was carried out as a part of the MPM-Flow project "Understanding flow slides in flood defences". It has received funding from the Netherlands Organisation for Scientific Research (NWO), Deltares, Royal Boskalis Westminster N.V., Van Oord Dredging and Marine Contractors, Rijkswaterstaat, and Stichting FloodControl IJkdijk. The authors are also grateful to Roel Tielen for his excellent work on BSMPM.

A List of abbreviations

BSMPM	B-Spline Material Point Method
CPDI	Convected Particle Domain Interpolation
DDMPM	Dual Domain Material Point Method
DOF	Degrees Of Freedom
FEM	Finite Element Method
GIMP	Generalized Interpolation Material Point
NWO	Nederlandse Organisatie voor Wetenschappelijk Onderzoek
MPM	Material Point Method
PPC	Particles Per Cell
RMS	Root Mean Square
TLS	Taylor Least Squares
ULFEM	Updated Lagrangian Finite Element Method

References

[1] D Sulsky, Z Chen, and HL Schreyer. A particle method for history-dependent materials. *Comput Methods in Appl Mech Eng*, 118(1-2):179–196, 1994.

[2] D Sulsky, SJ Zhou, and HL Schreyer. Application of a particle-in-cell method to solid mechanics. *Comput Phys Commun*, 87(1–2):236–252, 1995.

[3] SC Brenner and LR Scott. *The Mathematical Theory of Finite Element Methods*. Springer, New York, 3rd edition, 2008.

[4] M Martinelli and A Rohe. Modelling fluidisation and sedimentation using material point method. 1st Pan-American Congress on Computational Mechanics, pages 1–12, 2015.

[5] F Ceccato, L Beuth, PA Vermeer, and P Simonini. Two-phase material point method applied to the study of cone penetration. *Comput Geotech*, 80:440–452, 2016.

[6] D Shepard. A two-dimensional interpolation function for irregularly-spaced data. Proceedings of the 1968 23rd ACM national conference, pages 517–524, 1968.

[7] D Sulsky and M Gong. Improving the material-point method. Innovative Numerical Approaches for Multi-Field and Multi-Scale Problems, pages 217–240. Springer, 2016.

[8] M Gong. *Improving the Material Point Method*. PhD thesis, The University of New Mexico, 2015.

[9] SG Bardenhagen and EM Kober. The generalized interpolation material point method. *Comput Model Eng Sci*, 5(6):477–496, 2004.

[10] M Steffen, RM Kirby, and M Berzins. Decoupling and balancing of space and time errors in the material point method (mpm). *Int J Numer Methods Eng*, 82(10):1207–1243, 2010.

[11] A Sadeghirad, RM Brannon, and J Burghardt. A convected particle domain interpolation technique to extend applicability of the material point method for problems involving massive deformations. *Int J Numer Methods Eng*, 86(12):1435–1456, 2011.

[12] DZ Zhang, X Ma, and PT Giguere. Material point method enhanced by modified gradient of shape function. *J Comput Phys*, 230(16):6379–6398, 2011.

[13] M Steffen, RM Kirby, and M Berzins. Analysis and reduction of quadrature errors in the material point method (mpm). *Int J Numer Methods Eng*, 76(6):922–948, 2008.

[14] R Tielen, E Wobbes, M Möller, and L Beuth. A high order material point method. *Procedia Eng*, 175:265–272, 2017.

[15] AM Legendre. *Nouvelles méthodes pour la détermination des orbites des comètes*. F. Didot, 1805.

[16] H Luo, JD Baum, and R Löhner. A discontinuous galerkin method based on a taylor basis for the compressible flows on arbitrary grids. *J Comput Phys*, 227(20):8875–8893, 2008.

[17] TR Dhakal and DZ Zhang. Material point methods applied to one-dimensional shock waves and dual domain material point method with sub-points. *J Comput Phys*, 325:301–313, 2016.

[18] Y Gan, Z Sun, Z Chen, X Zhang, and Y Liu. Enhancement of the material point method using b-spline basis functions. *Int J Numer Methods Eng*, 113(3):411–431, 2017.

[19] LE Malvern. *Introduction to the Mechanics of a Continuous Medium*. Prentice-Hall, Englewood Cliffs, New Jersey, 1996.

[20] R Hill. Some basic principles in the mechanics of solids without a natural time. *J Mech Phys Solids*, 7(3):209–225, 1959.

[21] J Van Esch, D Stolle, and I Jassim. Finite element method for coupled dynamic flow-deformation simulation. 2nd International Symposium on Computational Geomechanics, 2011.

[22] K Terzaghi. *Erdbaumechanik auf bodenphysikalischer Grundlage*. F. Deuticke, Vienna, 1925.

[23] A Cromer. Stable solutions using the euler approximation. *Am J Phys*, 49(5):455–459, 1981.

[24] IKJ AL-Kafaji. *Formulation of a dynamic material point method (MPM) for geomechanical problems*. PhD thesis, Institut für Geotechnik der Universität Stuttgart, 2013.

[25] C De Boor. *A practical guide to splines. Applied Mathematical Sciences*. Springer, New York, 2001.

[26] RPWM Tielen. High-order material point method. Master's thesis, Delft University of Technology, 2016.

[27] KJ Bathe, E Ramm, and EL Wilson. Finite element formulations for large deformation dynamics analysis. *Int J Numer Methods Eng*, 9(2):353–386, 1975.

[28] A Verruijt. *An Introduction to Soil Dynamics*. Springer, Dordrecht, 2010.

[29] KH Xie and CJ Leo. Analytical solutions of one-dimensional large strain consolidation of saturated and homogeneous clays. *Comput Geotech*, 31:301–314, 2004.